Achieving a Record-High Yield Rate of 120.9 μg_{NH_3} $mg_{cat.}^{-1}$ h^{-1} for N$_2$ Electrochemical Reduction over Ru Single-Atom Catalysts

Zhigang Geng, Yan Liu, Xiangdong Kong, Pai Li, Kan Li, Zhongyu Liu, Junjie Du, Miao Shu, Rui Si,* and Jie Zeng*

The electrochemical reduction of N$_2$ into NH$_3$ production under ambient conditions represents an attractive prospect for the fixation of N$_2$. However, this process suffers from low yield rate of NH$_3$ over reported electrocatalysts. In this work, a record-high activity for N$_2$ electrochemical reduction over Ru single atoms distributed on nitrogen-doped carbon (Ru SAs/N-C) is reported. At −0.2 V versus reversible hydrogen electrode, Ru SAs/N-C achieves a Faradaic efficiency of 29.6% for NH$_3$ production with partial current density of −0.13 mA cm^{-2}. Notably, the yield rate of Ru SAs/N-C reaches 120.9 μg_{NH_3} $mg_{cat.}^{-1}$ h^{-1}, which is one order of magnitude higher than the highest value ever reported. This work not only develops a superior electrocatalyst for NH$_3$ production, but also provides a guideline for the rational design of highly active and robust single-atom catalysts.

Nitrogen is an essential building element for biomolecules such as proteins, nucleotides, and other biological compounds in plants and animals.[1–3] Although molecular nitrogen (N$_2$) is the major component on earth (78% in the atmosphere), it is nutritionally unavailable due to the highly stable N≡N covalent triple bond with the bond energy of 940.95 kJ mol^{-1}.[4–6] As such, high pressure and temperature (150–350 atm, 350–550 °C) are required to convert N$_2$ to available nitrogen-containing compounds such as NH$_3$ through Haber–Bosch process in industry.[7–10] The harsh condition of Haber–Bosch process

results in 1–2% of the world's annual energy supply consumption.[11,12] Moreover, the NH$_3$ synthesis through Haber–Bosch process requires hydrogen gas as source, which is generated from the steam reforming of natural gas with a large concomitant emission of CO$_2$.[13,14] In view of the fossil fuels shortage and global climate change, it is highly desired to explore a catalytic process that produces NH$_3$ using N$_2$ and earth-abundant hydrogen sources under ambient conditions.

Recently, a variety of sustainable routes for fixing N$_2$ to NH$_3$ have been developed by using biological nitrogenase,[15] photocatalysis,[16] and electrocatalysis.[17–20] As a strategy of NH$_3$ synthesis under the ambient reaction condition, electrochemical reduction of N$_2$ into NH$_3$ has attracted particular attention, because this process utilizes H$_2$O as hydrogen source and can be facilely controlled by altering the applied electrode potential. Thanks to the tremendous efforts from many research groups, numerous catalysts such as Ru,[18] Au,[21–23] poly(N-ethyl-benzene-1,2,4,5-tetracarboxylic diimide) with Li$^+$ incorporation,[24] N-doped porous carbon,[25] and Fe$_2$O$_3$/carbon nanotube[26] have been developed for N$_2$ electrochemical reduction. However, to date, the highest NH$_3$ yield rate among the reported electrocatalysts was only 23.8 μg_{NH_3} $mg_{cat.}^{-1}$ h^{-1} toward N$_2$ electrochemical reduction.[25] Therefore, the development of highly active electrocatalysts for NH$_3$ production is desirable but remains challenging.

Herein, we developed Ru single atoms on nitrogen-doped carbon (denoted as Ru SAs/N-C) which achieved record-high activity toward N$_2$ electrochemical reduction. At −0.2 V versus reversible hydrogen electrode (RHE), Ru SAs/N-C exhibited a Faradaic efficiency (FE) of 29.6% for NH$_3$ production with partial current density of −0.13 mA cm^{-2}. Notably, the yield rate of Ru SAs/N-C reached 120.9 μg_{NH_3} $mg_{cat.}^{-1}$ h^{-1}, which was one order of magnitude higher than the highest value ever reported. Moreover, Ru SAs/N-C also held high catalytic stability toward N$_2$ electrochemical reduction at different applied potentials.

Typically, Ru SAs/N-C was prepared via pyrolyzing the Ru-containing derivative of zeolitic imidazolate frameworks (ZIF-8). The synthetic procedure of Ru SAs/N-C is illustrated

Dr. Z. Geng, Y. Liu, X. Kong, Dr. P. Li, K. Li, Z. Liu, J. Du, Prof. J. Zeng
Hefei National Laboratory for Physical Sciences at the Microscale
Key Laboratory of Strongly-Coupled Quantum Matter Physics of Chinese Academy of Sciences
Department of Chemical Physics
University of Science and Technology of China
Hefei, Anhui 230026, P. R. China
E-mail: zengj@ustc.edu.cn
M. Shu, Prof. R. Si
Shanghai Synchrotron Radiation Facility
Shanghai Institute of Applied Physics
Chinese Academy of Sciences
Shanghai 201204, P. R. China
E-mail: sirui@sinap.ac.cn

**ADVANCED
SCIENCE NEWS**

www.advancedsciencenews.com
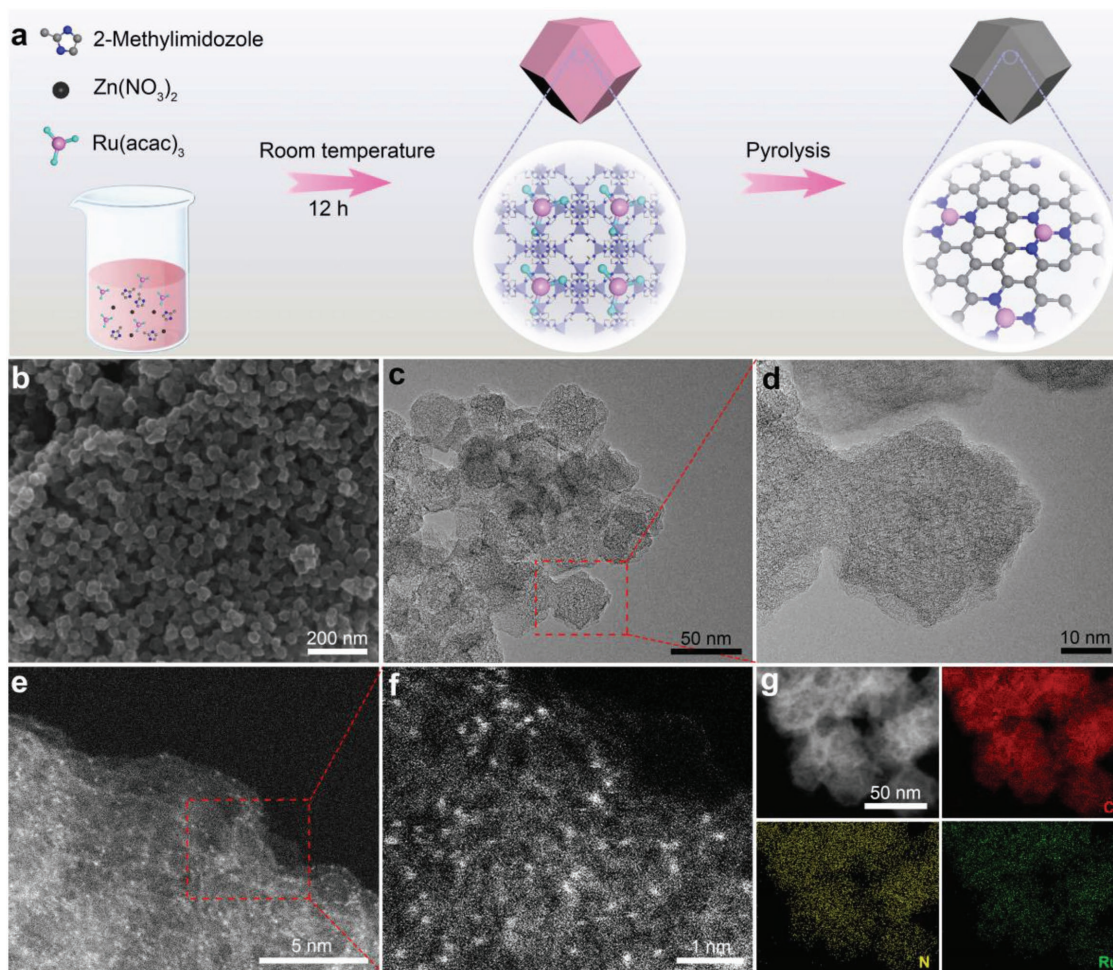
**ADVANCED
MATERIALS**

www.advmat.de

Figure 1. a) Scheme of the synthetic procedure for Ru SAs/N-C. b) A typical SEM image, c) TEM image, d) magnified TEM image, e) HAADF-STEM image, and f) magnified HAADF-STEM image of Ru SAs/N-C. g) HAADF-STEM image and corresponding EDS elemental mapping results for Ru SAs/N-C.

in **Figure 1**a. The Ru-containing derivative of ZIF-8 was synthesized through the standard synthetic route of ZIF-8 except for partial substitution of $Zn(NO_3)_2$ with $Ru(acac)_3$.[27,28] As shown in Figure S1 (Supporting Information), the derivative of ZIF-8 exhibited homogeneous rhombododecahedral morphology with an average size of 60 nm. After the derivative was pyrolyzed under N_2 flow at 900 °C for 3 h, Ru SAs/N-C was obtained. The Ru mass loading was determined to be 0.18% by inductively coupled plasma atomic emission spectroscopy (ICP-AES). As shown in the scanning electron microscopy (SEM) and transmission electron microscopy (TEM) images of Ru SAs/N-C, the original structure shrank into porous irregular rhombododecahedrons with an average size of 40 nm after pyrolysis process (Figure 1b–d). The high-angle annular dark field scanning transmission electron microscopy (HAADF-STEM) image and magnified HAADF-STEM image of Ru SAs/N-C demonstrate that individual Ru atoms were uniformly dispersed (Figure 1e,f). The HAADF-STEM image and the corresponding energy-dispersive X-ray spectroscopy (EDS) elemental mapping show the homogeneous distribution of the C, N, and Ru elements throughout the whole structure (Figure 1g).

For comparison, we also prepared Ru nanoparticles on the nitrogen-doped carbon (denoted as Ru NPs/N-C) with the Ru loading of 2.64% by increasing the molar ratio of $Ru(acac)_3$/$Zn(NO_3)_2$ to 1:1. The TEM image indicates that the average size of Ru nanoparticles in Ru NPs/N-C was 3.5 nm (Figure S2, Supporting Information).

To investigate the structures and compositions of Ru SAs/N-C and Ru NPs/N-C, we conducted a series of characterizations, including X-ray diffraction (XRD), X-ray photoelectron spectroscopy (XPS), and Raman measurements. **Figure 2**a shows the XRD spectra of Ru SAs/N-C and Ru NPs/N-C. Both Ru SAs/N-C and Ru NPs/N-C exhibited two broad peaks at 24.1° and 43.3° which were attributed to the (002) and (101) facets of graphite carbon, respectively (Figure S3, Supporting Information). The diffraction peaks of Ru NPs/N-C were well indexed to a hexagonal-close-packed crystal structure of Ru (JCPDS No. 06-0663). By contrast, the characteristic peak of Ru crystals disappeared in the XRD pattern of Ru SAs/N-C, further demonstrating the absence of Ru nanoparticles in Ru SAs/N-C. The XPS spectrum of Ru SAs/N-C and Ru NPs/N-C showed no peaks for Zn 2p, demonstrating that Zn^{2+} species in derivative
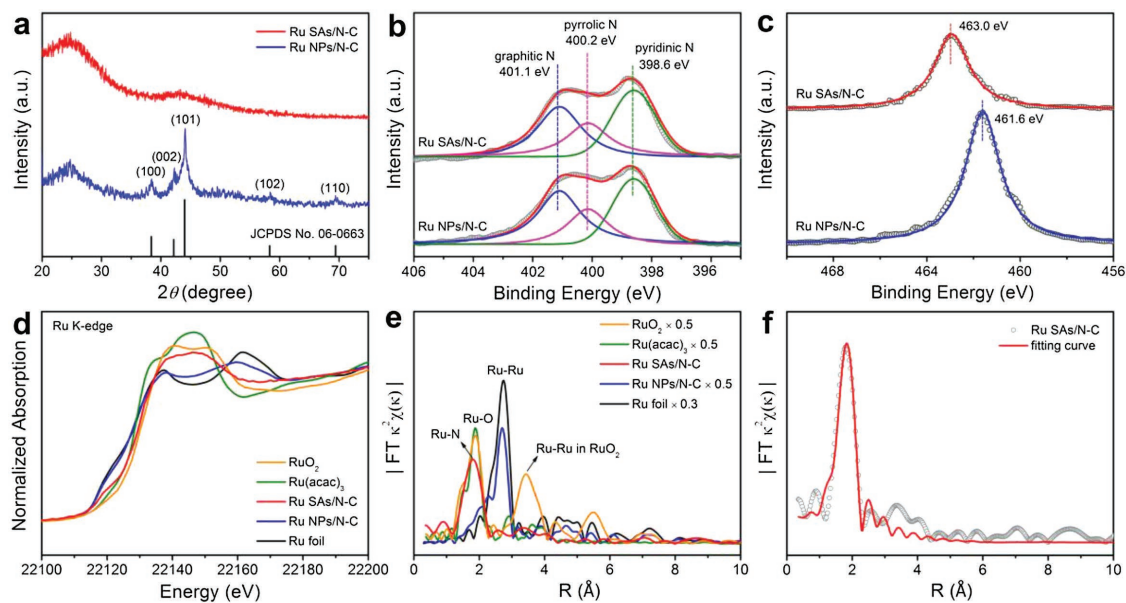
Figure 2. a) XRD patterns of Ru SAs/N-C and Ru NPs/N-C. XPS spectra of the b) N 1s and c) Ru $3p_{3/2}$ for Ru SAs/N-C and Ru NPs/N-C. d) Ru K-edge XANES spectra and e) EXAFS spectra for Ru SAs/N-C, Ru NPs/N-C, RuO_2, $Ru(acac)_3$, and Ru foil. f) EXAFS fitting curve for Ru SAs/N-C.

of ZIF-8 were evaporated during the pyrolysis process (Figure S4, Supporting Information).[29] In N 1s spectra of Ru SAs/N-C and Ru NPs/N-C, three peaks at 398.6, 400.2, and 401.1 eV were assigned to pyridinic N, pyrrolic N, and graphitic N, respectively (Figure 2b).[30] Meanwhile, the C−N peak at 286.5 eV were clearly recorded in C 1s spectra of Ru SAs/N-C and Ru NPs/N-C (Figure S5, Supporting Information). The XPS results indicate that the organic linkers in the derivative of ZIF-8 were transformed into nitrogen-doped carbon. Moreover, the Ru $3p_{3/2}$ peaks of Ru SAs/N-C and Ru NPs/N-C were located at 463.2 and 461.6 eV, which were attributed to the oxidized and metallic Ru, respectively (Figure 2c).[31] The defect structure of nitrogen-doped carbon in Ru SAs/N-C and Ru NPs/N-C was further investigated by Raman spectra. As shown in Figure S6 (Supporting Information), two peaks at 1350 and 1580 cm^{-1} corresponded to D band and G band of graphite carbon, respectively.[32] The intensity ratio of D band to G band (I_D/I_G) for Ru SAs/N-C was 1.01, which was similar to that (1.02) for Ru NPs/N-C. Accordingly, the frame of porous carbon in both samples possessed the similar degree of disorder for sp^2 carbon.

To further investigate the electronic and coordination structures of Ru SAs/N-C and Ru NPs/N-C, we conducted the X-ray absorption near-edge spectroscopy (XANES) and extended X-ray absorption fine structure (EXAFS) measurements. Figure 2d shows the Ru K-edge XANES profiles for Ru SAs/N-C, Ru NPs/N-C, RuO_2, $Ru(acac)_3$, and Ru foil. Ru SAs/N-C exhibited the similar energy absorption edge profiles with that of $Ru(acac)_3$ (Ru^{3+}) in a range between 22 110 and 22 130 eV. Moreover, we have further conducted the derivative profiles for XANES of Ru SAs/N-C, Ru NPs/N-C, RuO_2, $Ru(acac)_3$, and Ru foil. As shown in Figure S7 (Supporting Information), the derivative profile for XANES of Ru SAs/N-C exhibited a similar pre-edge structure ranging from 22 112 to 22 121 eV with that of $Ru(acac)_3$. The maximum XANES slopes

of both Ru SAs/N-C and $Ru(acac)_3$ were located at 22 129 eV. Therefore, the valence state of Ru species in Ru SAs/N-C was ≈+3. In contrast, the energy absorption edge profile of Ru NPs/N-C matched well with that of the Ru foil, demonstrating the metallic Ru species in Ru NPs/N-C. As shown in Figure 2e, EXAFS spectra for Ru SAs/N-C exhibited only a prominent peak at ≈2.04 Å which was attributed to Ru−N bonds. No significant contribution for metallic Ru and oxidized Ru_xO_y clusters was observed at longer distance above 2.50 Å, revealing the dispersion of isolated Ru atoms throughout the whole Ru SAs/N-C structure. As for Ru NPs/N-C, a typical peak located at 2.70 Å was observed, implying the formation of a Ru−Ru metallic bond. To further obtain the structure parameters of Ru in Ru SAs/N-C, we conducted a least-squares EXAFS fitting. When the EXAFS fitting parameter of the bond length was set to 2.04 Å with the coordination number of ≈3.4 (Table S1, Supporting Information), the fitting curve of Ru SAs/N-C perfectly matched with the EXAFS result (Figure 2f). Based on the above analysis, the Ru atom in Ru SAs/N-C was coordinated by N atoms.

To evaluate the electrochemical activity over Ru SAs/N-C and Ru NPs/N-C toward N_2 electrochemical reduction, we tested the cyclic voltammetry (CV) curves of Ru SAs/N-C and Ru NPs/N-C in both N_2-saturated and Ar-saturated 0.05 M H_2SO_4 electrolyte (Figure S8, Supporting Information). For Ru SAs/N-C, the current density in N_2-saturated electrolyte was higher than that in Ar-saturated electrolyte at the potential ranging from −0.15 to −0.50 V versus RHE, indicating that Ru SAs/N-C possessed catalytic activity toward N_2 electrochemical reduction. At the potential below −0.50 V versus RHE, the current density of Ru SAs/N-C in N_2-saturated electrolyte approximated to that in Ar-saturated electrolyte with the divergence below 0.09 mA cm^{-2}. In this case, the hydrogen evolution reaction became the primary process. By contrast, Ru NPs/N-C exhibited similar CV curves in both N_2-saturated and
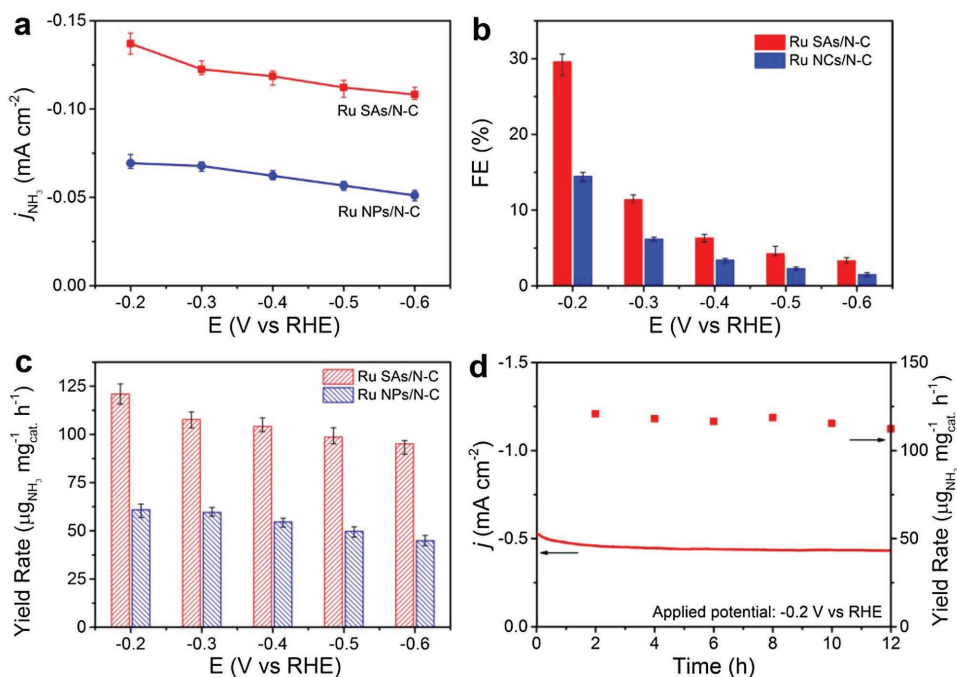
**ADVANCED
SCIENCE NEWS**

www.advancedsciencenews.com

**ADVANCED
MATERIALS**

www.advmat.de

Figure 3. a) Current densities for NH$_3$ production. b) FE and c) yield rate of NH$_3$ production at different applied potentials on Ru SAs/N-C and Ru NPs/N-C. d) 12 h durability test for Ru SAs/N-C toward N$_2$ electrochemical reduction at −0.2 V versus RHE.

Ar-saturated electrolytes, suggesting the low catalytic activity toward N$_2$ electrochemical reduction. The catalytic performance of Ru SAs/N-C and Ru NPs/N-C was further tested in N$_2$-saturated 0.05 M H$_2$SO$_4$ electrolyte toward N$_2$ electrochemical reduction. After a 12 h test for Ru SAs/N-C at −0.2 V versus RHE, the electrolyte was qualitatively detected by the Fourier transform infrared (FTIR) spectroscopy. As shown in Figure S9 (Supporting Information), the characteristic peak at 1450 cm^{-1} for NH$_4^+$ deformational vibration was observed, indicating the generation of NH$_3$ over Ru SAs/N-C during N$_2$ electrochemical reduction.[33] The concentration of NH$_4^+$ was also quantified via a calibrated indophenols blue method, which was in good agreement with the result determined by ion chromatography (Figures S10 and S11, Supporting Information). The production of hydrazine was below the detection limit, indicating the high selectivity for NH$_3$ over Ru SAs/N-C and Ru NPs/N-C (Figure S12, Supporting Information). **Figure 3**a shows the partial current density of Ru SAs/N-C and Ru NPs/N-C for NH$_3$ production. At all applied potentials, Ru SAs/N-C exhibited higher partial current density for NH$_3$ production than that of Ru NPs/N-C. Typically, at −0.2 V versus RHE, the partial current density of Ru SAs/N-C for NH$_3$ production reached −0.13 mA cm^{-2}, which was approximately twice that of Ru NPs/N-C. In addition, the FE of Ru SAs/N-C for NH$_3$ production was higher than that of Ru NPs/N-C at all applied potentials (Figure 3b). Remarkably, the FE of Ru SAs/N-C for NH$_3$ production reached 29.6% at −0.2 V versus RHE, which was 2.1-fold higher than that of Ru NPs/N-C. Moreover, we normalized the yield rate of NH$_3$ production based on the weight of catalysts. At −0.2 V versus RHE, Ru SAs/N-C exhibited a record-high yield rate of 120.9 μg$_{NH_3}$ mg$_{cat.}^{-1}$ h^{-1} for NH$_3$ production (Figure 3c). Notably, such value is more than one order

of magnitude higher than that of other electrocatalysts under the near-ambient conditions for NH$_3$ production up to date (**Table 1**).

To verify that NH$_3$ production over Ru SAs/N-C and Ru NPs/N-C was generated via N$_2$ electrochemical reduction process, we performed a series of control experiments. When the reaction proceeded in an Ar-saturated electrolyte at −0.2 V versus RHE for 2 h, the yields of NH$_3$ production for Ru SAs/N-C and Ru NPs/N-C were below detection limit (Figure S13, Supporting Information). As such, the NH$_3$ production did not derive from the self-electrolysis of catalysts. When Ru SAs/N-C was conducted in N$_2$-saturated 0.05 M H$_2$SO$_4$ electrolyte at open-circuit, no NH$_3$ production was detected, indicating the absence of NH$_3$ impurity in N$_2$ gas (Figure S13, Supporting Information). We also conducted the N$_2$ electrochemical reduction over pyrolyzed ZIF-8 to exclude the catalytic performance of nitrogen-doped carbon in Ru SAs/N-C (Figure S14, Supporting Information). At −0.2 V versus RHE, the pyrolyzed ZIF-8 exhibited a poor FE of 0.4% for NH$_3$ production with a low yield rate of 5.2 μg$_{NH_3}$ mg$_{cat.}^{-1}$ h^{-1}. As such, Ru single atoms in Ru SAs/N-C served as the active sites for N$_2$ electrochemical reduction. To confirm the origination of NH$_3$ production, we conducted an isotopic labeling experiment using ^{15}N$_2$ as the feeding gas. A distinguishable chemical shift of doublet coupling was attributed to ^{15}N in ^{15}NH$_4^+$ determined by ^{1}H NMR spectra (Figure S15, Supporting Information).[24] Therefore, the NH$_3$ production derived from N$_2$ electrochemical reduction. To explore the effect of the electrolyte, we measured CV curves in 0.05 M Na$_2$SO$_4$ and 0.1 M KOH electrolyte for both Ru SAs/N-C and Ru NPs/N-C. For Ru SAs/N-C, the current density in N$_2$-saturated electrolyte was higher than that in Ar-saturated electrolyte at the potential ranging from −0.15 to −0.50 V versus

**ADVANCED
SCIENCE NEWS**

www.advancedsciencenews.com

**ADVANCED
MATERIALS**

www.advmat.de

Table 1. Comparison of the N_2 electrochemical reduction activity for Ru SAs/N-C with other catalysts under near-ambient conditions.

Catalyst	Electrolyte	Potential	Yield rate		Ref.
			Area activity [μg_{NH_3} cm^{-2} h^{-1}]	Mass activity [μg_{NH_3} mg$_{cat.}^{-1}$ h^{-1}]	
Ru/C	2 M KOH	−1.1 V versus Ag/AgCl	0.21	–	[18]
Au/CeO$_x$-RGO	0.1 M HCl	−0.2 V versus RHE	–	8.3	[21]
Au nanorods	0.1 M KOH	−0.2 V versus RHE	1.65	–	[22]
Au cluster/TiO$_2$	0.1 M HCl	−0.2 V versus RHE	–	21.4	[23]
PEBCD/C	0.5 M Li$_2$SO$_4$	−0.7 V versus RHE	–	2.01	[24]
N-doped porous carbon	0.05 M H$_2$SO$_4$	−0.9 V versus RHE	9.47	23.8	[25]
Fe$_2$O$_3$-CNT	Diluted KHCO$_3$	−2.0 V versus Ag/AgCl	0.22	–	[26]
Ru SAs/N-C	0.05 M H$_2$SO$_4$	−0.2 V versus RHE	30.84	120.9	This work

RHE, irrespective of H_2SO_4, Na_2SO_4, and KOH solutions (Figure S16, Supporting Information). In addition, Ru NPs/N-C exhibited similar CV curves in N_2-saturated and Ar-saturated electrolyte regardless of different solutions. As shown in Figure S17 (Supporting Information), the FE of NH_3 production for Ru SAs/N-C in Na_2SO_4 and KOH solution was 29.1 and 29.4%, respectively, approximating to that (29.6%) in H_2SO_4 solution at −0.2 V versus RHE, while the divergence of FE in three types of solutions was within the error for Ru NPs/N-C. Therefore, the electrolyte solution was not critical in our work. We further calculated the turnover frequency (TOF) numbers of Ru SAs/N-C and Ru NPs/N-C based on the surface Ru atoms (Figure S18, Supporting Information). Notably, the TOF number of Ru SAs/N-C was 376 h^{-1}, which was about ten times larger than that (35 h^{-1}) of Ru NPs/N-C at −0.2 V versus RHE. In addition, the durability of Ru SAs/N-C was tested by scanning at a constant potential of −0.2 V versus RHE for 12 h (Figure 3d). Ru SAs/N-C exhibited less than 7% decay of yield rate for NH_3 production during a 12 h potentiostatic test (Figure S19, Supporting Information). After the electrolysis, the Ru single atoms were still atomically dispersed on the nitrogen-doped carbon (Figure S20, Supporting Information).

The intrinsic reason of high catalytic performance for Ru SAs/N-C was further investigated. We conducted N_2 temperature-programmed desorption (N_2-TPD) for Ru SAs/N-C and Ru NPs/N-C. As shown in **Figure 4**a, both Ru SAs/N-C and Ru NPs/N-C exhibited a peak at 196 °C, which was attributed to the chemical adsorption of N_2 on pyrolyzed ZIF-8 (Figure S21, Supporting Information). The other desorption peak for Ru SAs/N-C was located at 340 °C, which was assigned to the chemical adsorption of N_2 on Ru species. By comparison, the peak for N_2 chemical adsorption was located at 271 °C for Ru NPs/N-C. As such, the binding strength of N_2 on Ru SAs/N-C was stronger than that on Ru NPs/N-C. The strong binding of N_2 on Ru SAs/N-C indicated the facilitated adsorption of N_2, thus resulting in high activity of Ru SAs/N-C. To provide a theoretical insight into the reaction mechanism, we calculated the Gibbs free energy (*G*) for each step involved in the N_2 reduction at 0 V versus RHE on Ru$_1$−N$_3$, Ru$_1$−N$_4$, and Ru (101). As shown in Figure 4b and Figure S22 (Supporting Information), the variation in Gibbs free-energy (Δ*G*) from *NNH to *NNH$_2$ is 0.12 eV, which is more negative than that (0.60 eV) from *NNH to *NHNH for Ru$_1$−N$_3$ (Figures S23 and S24, Supporting Information). As such, the N_2 electrochemical reduction for Ru$_1$−N$_3$ undergoes the distal pathway rather than the alternating pathway. In addition, the reaction over Ru$_1$−N$_4$ also experiences the distal pathway according to the Δ*G* of the partial elementary reaction intermediates (Figure 4b and
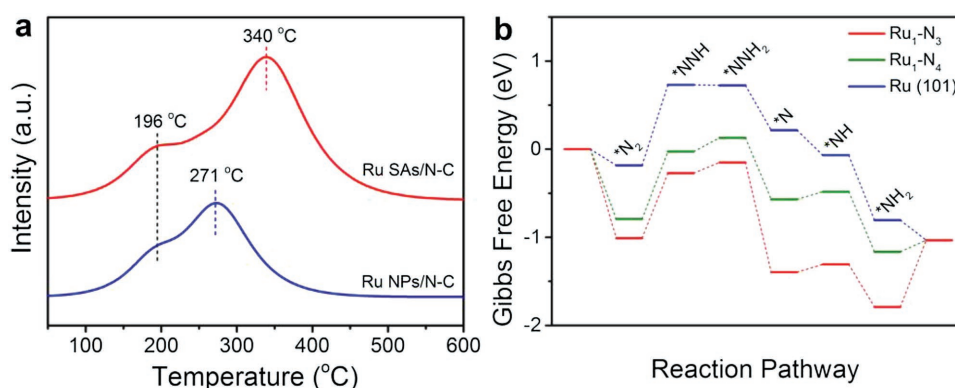

Figure 4. a) The N_2-TPD profiles of Ru SAs/N-C and Ru NPs/N-C. b) Free energy diagram of the N_2 electrochemical reduction with a distal pathway on Ru$_1$−N$_3$, Ru$_1$−N$_4$, and Ru (101). * represents an adsorption site.

Figure S22, Supporting Information). As shown in Figure 4b, the N_2 dissociation (from *N_2 to *NNH) exhibits the highest energy barrier among all the steps on either Ru SAs/N-C or Ru (101). Accordingly, N_2 dissociation serves as the rate-limiting step. Furthermore, the ΔG for N_2 dissociation on Ru_1-N_3 and Ru_1-N_4 are 0.73 and 0.77 eV, respectively, which are lower than that (0.91 eV) on Ru (101). As such, Ru SAs/N-C promotes N_2 dissociation, thereby resulting in enhanced activity relative to Ru NPs/N-C.

In conclusion, Ru SAs/N-C has been demonstrated to serve as a highly efficient electrocatalyst for N_2 electrochemical reduction. At −0.2 V versus RHE, Ru SAs/N-C exhibited a FE of 29.6% for NH_3 production with partial current density of −0.13 mA cm^{-2}. Notably, the yield rate of Ru SAs/N-C reached 120.9 μg_{NH_3} mg$_{cat.}^{-1}$ h^{-1}, which was one order of magnitude higher than the highest value ever reported. This work provides a guideline for the generation of atomically dispersed uniform single atomic materials and paves a new avenue for further research in the application of single atomic catalysts toward N_2 electrochemical reduction.

Supporting Information

Supporting Information is available from the Wiley Online Library or from the author.

Conflict of Interest

The authors declare no conflict of interest.

Keywords

[1] H. Li, J. Shang, Z. Ai, L. Zhang, *J. Am. Chem. Soc.* **2015**, *137*, 6393.

[2] H. Hirakawa, M. Hashimoto, Y. Shiraishi, T. Hirai, *J. Am. Chem. Soc.* **2017**, *139*, 10929.

[3] V. Kyriakou, I. Garagounis, E. Vasileiou, A. Vourros, M. Stoukides, *Catal. Today* **2017**, *286*, 2.

[4] S. Wang, X. Hai, X. Ding, K. Chang, Y. Xiang, X. Meng, Z. Yang, H. Chen, J. Ye, *Adv. Mater.* **2017**, *29*, 1701774.

[5] X. Chen, N. Li, Z. Kong, W.-J. Ong, X. Zhao, *Mater. Horiz.* **2018**, *5*, 9.

[6] C. J. M. van der Ham, M. T. M. Koper, D. G. H. Hetterscheid, *Chem. Soc. Rev.* **2014**, *43*, 5183.

[7] M. Kitano, Y. Inoue, Y. Yamazaki, F. Hayashi, S. Kanbara, S. Matsuishi, T. Yokoyama, S.-W. Kim, M. Hara, H. Hosono, *Nat. Chem.* **2012**, *4*, 934.

[8] M. Ali, F. Zhou, K. Chen, C. Kotzur, C. Xiao, L. Bourgeois, X. Zhang, D. R. MacFarlane, *Nat. Commun.* **2016**, *7*, 11335.

[9] D. Yang, T. Chen, Z. Wang, *J. Mater. Chem. A* **2017**, *5*, 18967.

[10] C. Guo, J. Ran, A. Vasileff, S.-Z. Qiao, *Energy Environ. Sci.* **2018**, *11*, 45.

[11] I. Rafiqul, C. Weber, B. Lehmann, A. Voss, *Energy* **2005**, *30*, 2487.

[12] J. G. Chen, R. M. Crooks, L. C. Seefeldt, K. L. Bren, R. M. Bullock, M. Y. Darensbourg, P. L. Holland, B. Hoffman, M. J. Janik, A. K. Jones, M. G. Kanatzidis, P. King, K. M. Lancaster, S. V. Lymar, P. Pfromm, W. F. Schneider, R. R. Schrock, *Science* **2018**, *360*, 873.

[13] Y. Abghoui, A. L. Garden, J. G. Howalt, T. Vegge, E. Skúlason, *ACS Catal.* **2016**, *6*, 635.

[14] J. H. Montoya, C. Tsai, A. Vojvodic, J. K. Nørskov, *ChemSusChem* **2015**, *8*, 2180.

[15] T. J. Del Castillo, N. B. Thompson, J. C. Peter, *J. Am. Chem. Soc.* **2016**, *138*, 5341.

[16] D. Zhu, L. Zhang, R. E. Ruther, R. J. Hamers, *Nat. Mater.* **2013**, *12*, 836.

[17] B. M. Lindley, A. M. Appel, K. Krogh-Jespersen, J. M. Mayer, A. J. M. Miller, *ACS Energy Lett.* **2016**, *1*, 698.

[18] V. Kordali, G. Kyriacou, Ch. Lambrou, *Chem. Commun.* **2000**, *17*, 1673.

[19] R. Lan, S. Tao, *RSC Adv.* **2013**, *3*, 18016.

[20] R. Lan, J. T. S. Irvine, S. Tao, *Sci. Rep.* **2013**, *3*, 1145.

[21] S.-J. Li, D. Bao, M.-M. Shi, B.-R. Wulan, J.-M. Yan, Q. Jiang, *Adv. Mater.* **2017**, *29*, 1700001.

[22] D. Bao, Q. Zhang, F.-L. Meng, H.-X. Zhong, M.-M. Shi, Y. Zhang, J.-M. Yan, Q. Jiang, X.-B. Zhang, *Adv. Mater.* **2017**, *29*, 1604799.

[23] M.-M. Shi, D. Bao, B.-R. Wulan, Y.-H. Li, Y.-F. Zhang, J.-M. Yan, Q. Jiang, *Adv. Mater.* **2017**, *29*, 1606550.

[24] G.-F. Chen, X. Cao, S. Wu, X. Zeng, L.-X. Ding, M. Zhu, H. Wang, *J. Am. Chem. Soc.* **2017**, *139*, 9771.

[25] Y. Liu, Y. Su, X. Quan, X. Fan, S. Chen, H. Yu, H. Zhao, Y. Zhang, J. Zhao, *ACS Catal.* **2018**, *8*, 1186.

[26] S. Chen, S. Perathoner, C. Ampelli, C. Mebrahtu, D. Su, G. Centi, *Angew. Chem., Int. Ed.* **2017**, *56*, 2699.

[27] R. Banerjee, A. Phan, B. Wang, C. Knobler, H. Furukawa, M. O'Keeffe, O. M. Yaghi, *Science* **2008**, *319*, 939.

[28] X.-C. Huang, Y.-Y. Lin, J.-P. Zhang, X.-M. Chen, *Angew. Chem., Int. Ed.* **2006**, *45*, 1557.

[29] T. Liu, D. Liu, F. Qu, D. Wang, L. Zhang, R. Ge, S. Hao, Y. Ma, G. Du, A. M. Asiri, L. Chen, X. Sun, *Adv. Energy Mater.* **2017**, *7*, 1700020.

[30] Y. Zheng, Y. Jiao, L. H. Li, T. Xing, Y. Chen, M. Jaroniec, S. Z. Qiao, *ACS Nano* **2014**, *8*, 5290.

[31] C. Zhang, J. Sha, H. Fei, M. Liu, S. Yazdi, J. Zhang, Q. Zhong, X. Zou, N. Zhao, H. Yu, Z. Jiang, E. Ringe, B. I. Yakobson, J. Dong, D. Chen, J. M. Tour, *ACS Nano* **2017**, *11*, 6930.

[32] S. Wang, L. Zhang, Z. Xia, A. Roy, D. W. Chang, J.-B. Baek, L. Dai, *Angew. Chem., Int. Ed.* **2012**, *51*, 4209.

[33] J. Yuan, J. Yang, H. Ma, C. Liu, *Microporous Mesoporous Mater.* **2016**, *222*, 202.